Swift evaluation of electron density profiles obtained by the Alkali Beam Emission Spectroscopy technique using linearized reconstruction

M Vécsei,[1, a)] G Anda,[1] O Asztalos,[1] D Dunai,[1] S Hegedűs,[1] D Nagy,[1] M Otte,[2] G I Pokol,[1] S Zoletnik,[1] and the W7-X team[2, b)]

[1)] *Centre for Energy Research, Konkoly-Thege Miklós út 29-33, 1121 Budapest, Hungary*

[2)] *Max-Planck Institute for Plasma Physics, Wendelsteinstrasse 1, 17491 Greifswald, Germany*

(Dated: 15 December 2021)

A method is presented for the swift reconstruction of electron density profiles measured by the Alkali Beam Emission Spectroscopy. It is based on the linearization of the governing rate equations and leads to a direct calculation for obtaining the profiles. The uncertainties of the measurement are incorporated into the problem through the utilization of Tikhonov regularization and the generalized least squares method. An approximation for the uncertainty of the reconstructed density data is calculated as well. The applicability of the method is tested against both simulated and real experimental results of the W7-X stellarator.

Keywords: fusion plasma diagnostics, beam emission spectroscopy, experimental data analysis

I. INTRODUCTION

Alkali beam spectroscopy (A-BES)[?] is a technique utilized in a number of fusion experiments[? ? ? ? ? ? ?] for the analysis of edge density profiles of magnetically confined plasmas. The diagnostic injects a high-energy atomic beam into the plasma[?] . The photons generated through the collisional excitation and subsequent de-excitation of the constituent atoms of the beam are observed by an optical detector system[? ?] . The system is tuned at detecting the photons emitted during the de-excitation from the first excited state to the ground state of the atoms. Therefore, the intensity of the light can be assumed to scale with the occupation level of the first excited state. Since the occupation of the energy levels along the beam line is governed by a rate equation, describing the collisions with plasma constituents and the spontaneous de-excitation process, the light profile along the beam is affected by the density of the plasma. By assuming that all other relevant parameters of the plasma are known from other diagnostics, the electron density profile along the beam can be reconstructed from the A-BES data by solving a transformed version of the rate equation. Due to the loss term in the rate equations mainly corresponding to the ionizing collisions, the beam attenuates as it propagates through the plasma. The A-BES diagnostic is therefore most sensitive at the Scrape-Off Layer (SOL). Current systems are capable of producing sufficient data for resolving physical processes with a time resolution in the order of $50\mu s$. Thus, the diagnostic can be applied to the analysis of transport processes at the plasma edge (e.g.[? ? ? ? ?]).

The density profiles from the detected light signals are usually reconstructed with a Bayesian approach[?] . This method determines the density profile by maximizing a posterior probability distribution. This is defined as the probability that a certain density profile is the source of the measured light profile. The robustness of this method is supported by the possibility of including measurement errors and additional information, such as data from other diagnostics, into the calculations. Nevertheless, this approach is iterative and the run time of the density reconstruction can become considerable. Hence, alternative approaches are useful to obtain fast approximate results to the equation. One approach is based on neural networks[?] which is able to obtain results in tens of microseconds running on GPU. However, approximating the uncertainty of the reconstructed density profiles is not straightforward in this case. The aim of the current study is to present an alternative approach retaining the mathematical form of the problem and allowing the approximation of the uncertainty of the reconstructed density profiles via the error propagation of the covariance matrix of the light profile.

The presented method is based on the linearization of the rate equation using an already known solution sufficiently close to the experimental data. The problem is consequently reduced to the solution of a matrix equation. The solution approximating the experimental data is found in a database of known solutions by a search algorithm. The measurement errors are incorporated to the equations as well with the generalized least squares method[?] . Tikhonov regularization is used for introducing priors to the problem[?] . Moreover, a conservative approximation for the uncertainty of the reconstructed density data is developed. This is based on the common error propagation formalism for linear transformations. The paper is structured as follows: Section II briefly presents the A-BES diagnostic at the Wendelstein 7-X stellarator. The data from this diagnostic has been used for the current study. The rate equations are also summarized in this section. The equations used for the density reconstruction algorithm are summarized in section III. The validity of the method and a few examples using experimental data are discussed in section IV. Finally, a summary of the results is presented in section V.

[a)] E-mail: vecsei.miklos@ek-cer.hu

[b)] See the authors list in T. Klinger et al., "Overview of first Wendelstein 7-X high-performance operation", Nucl. Fusion 112004 (2019)

II. THE ALKALI BEAM EMISSION SPECTROSCOPY DIAGNOSTIC

A. Diagnostic setup at W7-X

The A-BES system has been installed at W7-X in 2017[?] and is located at a torodial angle of $\phi = 72^0$ of the stellarator. The confining magnetic field has its maximal vertical and smallest horizontal elongation at this toroidal cross section. The diagnostic is capable of injecting sodium beam with an energy up to 60 keV and ion equivalent neutral current of $1mA$. During the experiments, the beam has been injected at a fixed energy of 40 keV from the low-field side in radial direction along the midplane of the stellarator at port AEA21. High-quality background-corrected beam emission light profiles can be obtained with an approximately $50\,\mu$s time resolution by a fast modulation of the beam.

The emitted light is detected with a detector system located at port AEB20, approximately vertically above the region of interest for the diagnostic. The optical system detects the 588.9 nm photons emitted during the 3p-3s transition of the sodium atoms. The photon flux is measured at 40 points along a radial line with a spatial resolution of approximately 5mm, at a camera sampling rate of 2MHz. The system utilizes both avalanche photodiodes (APD) and multi-pixel photon counters (MPPC). A small percentage of the light is diverted to a CMOS camera and is used for monitoring the beam and for spatial calibration. An overview of the diagnostic geometry is shown in Fig. 1.

For illustrative purposes, the raw signal data of two of the measurement channels is shown in Fig. 2. The modulation of the alkali beam, consisting of periodically diverting it from entering the plasma, is clearly visible in both cases. The light profiles corresponding to the sodium beam are calculated by taking the difference between the mean signal values during the "beam on" and the long "beam off" phases. (The $10\mu s$ long beam on and beam off phases shown in Fig. 2 depict the fastest achievable modulation by the diagnostic hardware.) The variation of the signal during either phase of the beam injection is interpreted as noise. Furthermore, the data obtained during the rise and fall times of the signals is omitted from the data analysis. The SNR of the APD channel is estimated to be in the order of $10^3 - 10^4$ during the experiment, while for the MPPC channel it is $10^1 - 10^2$. The lower SNR of the more advanced MPPC detector[?] is due to the lower photon flux in the far SOL, where the channel is used. (The eight MPPC measurement channels are located at major radii interval of approximately $[6.27, 6.30]$ in the current system.)

B. Rate equations

The occupation of the energy levels of the sodium beam atoms is defined by the following rate equation[?] .

$$\frac{d\boldsymbol{N}}{dz} = \frac{1}{v}\boldsymbol{N}\cdot(n_e R_e + n_p R_p + n_Z R_Z + A), \quad (1)$$

$$\boldsymbol{N} = (N_1, N_2, N_3, N_4, ...) = (n_{3s}, n_{3p}, n_{4s}, n_{3d}, ...) \quad (2)$$

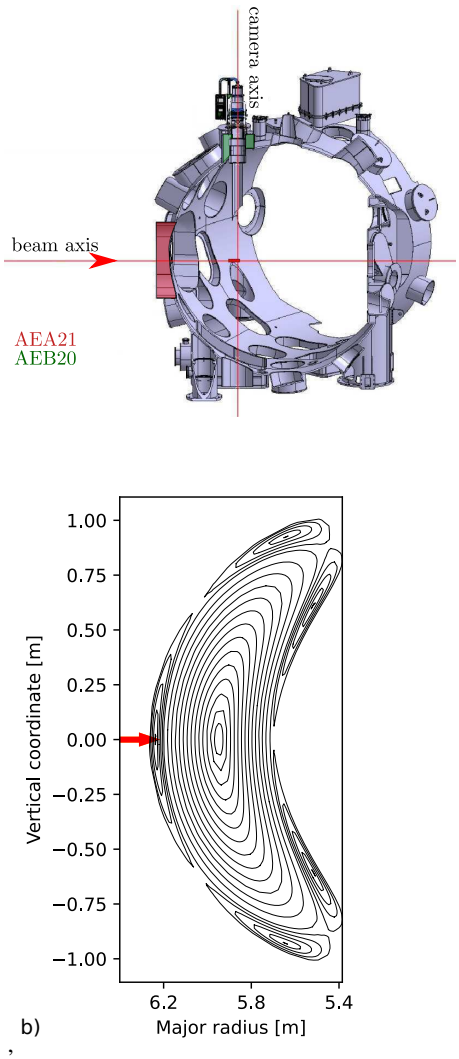

FIG. 1: a) The layout of the A-BES system at W7-X [*M Vécsei et al. P4.1021, 45th EPS Conference on Plasma Physics, 2018; licensed under a Creative Commons Attribution (CC BY) license.*] and b) a toroidal cross-section of the magnetic flux surfaces for the standard magnetic configuration at the beam location.

where n_e, n_p and n_Z represent the electron, proton and impurity densities of the plasma. The coordinate along the beam axis is denoted by z. The vector $\boldsymbol{N} = (n_{3s}, n_{3p}, n_{4s}, n_{3d}, ..)$ is a vector of the occupation numbers of the energy levels of the sodium atoms along the beam. The scalar beam velocity is given by v, while $R_{e/p/Z}$ are the collisional rate matrices for excitation, de-excitation and ionization. The matrix for the spontaneous de-excitation is given by A. Assuming quasi-neutrality for the plasma, one can reduce the equation to the following form:

$$\frac{d\boldsymbol{N}}{dz} = \frac{1}{v}\boldsymbol{N}\cdot(n_e R + A). \quad (3)$$

Here, all of the collisional processes are summarized in R. The collisional rate matrix is dependent on the effective ion

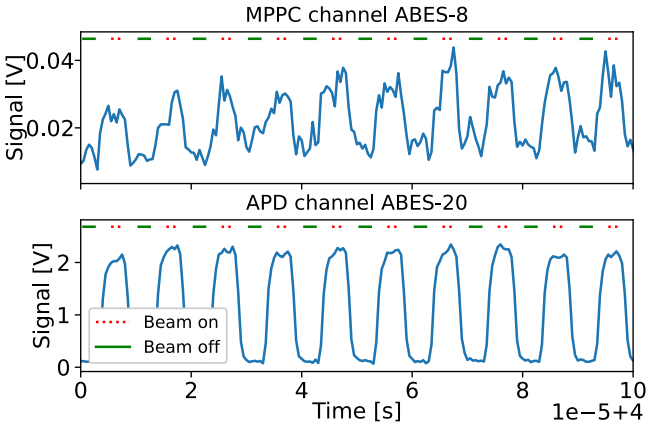

FIG. 2: The raw signals for experiment 20181017.021 of an APD and an MPPC channel located at major radii 6.201m and 6.268m, respectively.

charge, Z_{eff}, impurity ion charge and the electron and ion temperatures. These parameters are assumed to be known from other independent diagnostics. It is noted that for alkali beams, R is generally only weakly dependent on these quantities.

III. THE DENSITY RECONSTRUCTION ALGORITHM

A. Linear approximation of the rate equation

The reconstruction of the electron density profiles requires solving Eq. (3) for $n_e(z)$. Moreover, only the second element of $\boldsymbol{N}(z)$, i.e. $N_2(z)$ is known from the measurements, as it corresponds to the measured light profile. Other elements of this vector therefore have to be either transformed out of the equations or are also obtained by the density reconstruction algorithm.

For this study, a database consisting of known $\boldsymbol{N}^0$ solutions for the rate equation for different n_e^0 profiles is used to solve the problem. The experimental data $N_2(z)$ is used to find a similar light profile in the database and the rate equations are subsequently linearized along this solution in the database. Formally, one assumes that one has already obtained a solution to the problem

$$\frac{d\boldsymbol{N^0}}{dz} = \frac{1}{v}\boldsymbol{N}^0 \cdot (n_e^0 R + A). \tag{4}$$

Here, v, R and A are identical to the parameters of Eq. (3). Nevertheless, $\boldsymbol{N}^0$ and n_e^0 are only assumed to be close to the measurement data, as clarified later. Introducing $\boldsymbol{\delta N}$ and δn_e as

$$\begin{aligned} \boldsymbol{N} &\equiv \boldsymbol{N}^0 + \boldsymbol{\delta N}, \\ n_e &\equiv n_e^0 + \delta n_e, \end{aligned} \tag{5}$$

one can transform Eq. (3) to the form

$$\frac{d\left(\boldsymbol{N^0}+\boldsymbol{\delta N}\right)}{dz} = \frac{1}{v}\left(\boldsymbol{N^0}+\boldsymbol{\delta N}\right)\cdot\left[\left(n_e^0+\delta n_e\right)R + A\right], \tag{6}$$

$$\frac{d\boldsymbol{\delta N}}{dz} = \frac{1}{v}\delta n_e \boldsymbol{N^0}\cdot R + \frac{1}{v}\delta n_e \boldsymbol{\delta N}\cdot R + \frac{1}{v}\boldsymbol{\delta N}\cdot\left(n_e^0 R + A\right), \tag{7}$$

$$\frac{d\boldsymbol{\delta N}}{dz} \approx \frac{1}{v}\delta n_e \boldsymbol{N^0}\cdot R + \frac{1}{v}\boldsymbol{\delta N}\cdot\left(n_e^0 R + A\right). \tag{8}$$

Equation (7) has been obtained by substituting Eq. (4) to Eq. (6). In order to arrive at Eq. (8), one needs to assume that $\delta n_e \boldsymbol{\delta N}\cdot R \ll \delta n_e \boldsymbol{N^0}\cdot R + \boldsymbol{\delta N}\cdot\left(n_e^0 R + A\right)$. This requires that both $\boldsymbol{N}^0$ and n_e^0 are close to $\boldsymbol{N}$ and n_e. A sufficient condition for reducing the problem to Eq. (8) reads as

$$\boldsymbol{\delta N} \ll \boldsymbol{N^0} \text{ and } \delta n_e \ll n_e. \tag{9}$$

B. Incorporation of the measurement errors

In order to utilize Eq. (8) for processing measurement data, it is necessary that the measurement errors are also incorporated into the equations. A possible approach to this problem is summarized in the following. Firstly, the location of the measurement points along the light profile are introduced as z_1, z_2, ..., z_k The derivation is approximated with the finite difference method:

$$\frac{d\boldsymbol{\delta N}}{dz} \approx \frac{\boldsymbol{\delta N}|_{z_{i+1}} - \boldsymbol{\delta N}|_{z_i}}{z_{i+1} - z_i}, \tag{10}$$

where the $\boldsymbol{\delta N}|_{z_i} \equiv \boldsymbol{\delta N}(z = z_i)$ notation was introduced. Substituting this to the equation and writing the right-hand side in its implicit form leads to

$$\frac{\boldsymbol{\delta N}|_{z_{i+1}} - \boldsymbol{\delta N}|_{z_i}}{z_{i+1} - z_i} = \delta n_e|_{z_{i+1}} \left(\frac{1}{v}\boldsymbol{N^0}\cdot R\right)|_{z_{i+1}} + \frac{1}{v}\boldsymbol{\delta N}|_{z_{i+1}}\cdot(n_e^0 R + A)|_{z_{i+1}}, \tag{11}$$

This is a linear equation system for the values of $\boldsymbol{\delta N}$ and δn_e at the measurement points. In order to transform it to a more compact form, firstly the following notations are introduced,

$$\boldsymbol{U} \equiv \frac{1}{v}\boldsymbol{N^0}\cdot R \text{ and } S \equiv \frac{1}{v}\left(n_e^0 R + A\right). \tag{12}$$

Secondly, the order of the elements of $\boldsymbol{\delta N}$, $\boldsymbol{U}$ and S are changed such that the elements corresponding to the first excited state of the beam atoms are moved to the end of the vectors and similarly to the last row and column of S:

$$\boldsymbol{\delta N'} = (\delta N_1, \delta N_3, ..., \delta N_2) \equiv (\boldsymbol{\delta N_p}, \delta N_2) \tag{13}$$

$$\boldsymbol{U'} = (U_1, U_3, ..., U_2) \equiv (\boldsymbol{U_p}, U_2), \tag{14}$$

$$S' = \begin{pmatrix} S_{11} & S_{13}, & \dots & S_{12}, \\ S_{31} & S_{33}, & \dots & S_{32} \\ \dots & \dots & \dots & \dots \\ S_{21}, & S_{23}, & \dots & S_{22} \end{pmatrix} \equiv \begin{pmatrix} S_p & \boldsymbol{S}_{p2} \\ \boldsymbol{S}_{2p} & S_{22} \end{pmatrix}. \tag{15}$$

The vectors $\boldsymbol{\delta N_p}$, $\boldsymbol{U_p}$, $\boldsymbol{S}_{p2}$, $\boldsymbol{S}_{2p}$ and the matrix S_p were introduced to denote blocks of the $\boldsymbol{\delta N'}$, $\boldsymbol{U'}$ and S' variables. With this, the equations are transformed to

$$\begin{aligned}\frac{\boldsymbol{\delta N_p}|_{z_{i+1}} - \boldsymbol{\delta N_p}|_{z_i}}{z_{i+1}-z_i} =& \delta n_e|_{z_{i+1}} \boldsymbol{U_p}|_{z_{i+1}} + \boldsymbol{\delta N_p}|_{z_{i+1}} \cdot S_p|_{z_{i+1}} \\ &+ \delta N_2|_{z_{i+1}} \boldsymbol{S}_{2p}|_{z_{i+1}}, \qquad (16)\\ \frac{\delta N_2|_{z_{i+1}} - \delta N_2|_{z_i}}{z_{i+1}-z_i} =& \delta n_e|_{z_{i+1}} U_2|_{z_{i+1}} + \boldsymbol{\delta N_p}|_{z_{i+1}} \cdot \boldsymbol{S}_{p2}|_{z_{i+1}} \\ &+ \delta N_2|_{z_{i+1}} S_{22}|_{z_{i+1}} \qquad (17)\end{aligned}$$

Using this form, the values of $\boldsymbol{\delta N_p}|_{z_{i+1}}$ and $\delta n_e|_{z_{i+1}}$ can be calculated from the values of $\boldsymbol{\delta N_p}|_{z_i}$ and $\delta n_e|_{z_i}$. Thus, the problem can be solved if the boundary values of $\boldsymbol{\delta N_p}$ and δn_e are known. Nevertheless, the uncertainty of the light measurement is not yet included into the calculation and a direct application of the above formula would lead to unreliable results. (This is due to Eqs. (16) and (17) containing the derivative of δN_2 and thus being sensitive to noise on this data.) A common approach to solving this problem is the Maximum Entropy method[?] . Nevertheless, for the current study a mathematically less robust but direct approach is utilized in order to obtain the approximative values of the density profiles rapidly. Firstly, the generalized least squares method[?] is utilized for incorporating the measurement errors. This method is used for linear regression problems to fit parameters to correlated measurement data. For this purpose, all of the linear Eqs. (16) and (17) are summarized in a matrix form of the linear equations

$$\boldsymbol{W} = T \cdot \begin{pmatrix} \boldsymbol{\delta N_p}|_{z_2} \\ \delta n_e|_{z_2} \\ \boldsymbol{\delta N_p}|_{z_3} \\ \dots \\ \delta n_e|_{z_k} \end{pmatrix}. \qquad (18)$$

For this equation, the boundary conditions $\boldsymbol{\delta N_p}|_{z_1} = \boldsymbol{0}$ and $\delta n_e|_{z_1} = 0$ were assumed. This is a reasonable assumption, as usually the first channel of the measurement is detecting the light data outside the last closed magnetic flux surface (LCFS), where the electron density is small and the beam atoms are in ground state. The notation T was introduced for brevity and it corresponds to the square matrix governing the equation system. The vector $\boldsymbol{W}$ contains the $\delta N_2|_{z_i}$ scalars and their products with $S_{22}|_{z_i}$ and $\boldsymbol{S}_{2p}|_{z_i}$. A common approach to finding a unique and stable solution to equations of form (18) is the utilization of the least squares method together with Tikhonov regularization[?] . Tikhonov regularization introduces prior knowledge about the properties of the solution of the equation to stabilize the problem, while the least squares method allows one to find a unique solution, optimal in L^2 norm. The former step is performed by adding additional independent linear equations to the equation system (18), containing the assumptions about the solution. For instance, a common linear equation[?] for a prior dampening the oscillation of the reconstructed density profile reads as

$$\begin{aligned}&\left.\frac{\partial^2 \delta n_e}{\partial z^2}\right|_{z_i} = 0, \text{ thus} \\ &\left[\frac{\delta n_e|_{z_{i+1}} - \delta n_e|_{z_i}}{z_{i+1}-z_i} - \frac{\delta n_e|_{z_i} - \delta n_e|_{z_{i-1}}}{z_i - z_{i-1}}\right] \frac{2}{z_{i+1}-z_{i-1}} \approx 0. \qquad (19)\end{aligned}$$

If Eq. (19) were to be taken as a strict condition for the solution, then it would lead to linear profiles for the density perturbation. Nevertheless, by the usage of the least squares method and regularization parameters, the magnitude of the effect Eq. (19) has on the results can be tuned. In this sense, it is to be understood as an additional correction for smoothening the results. Similar linear equations of $\delta n_e|_{z_i}$ and $\boldsymbol{\delta N_p}|_{z_i}$ can be added to Eq. (18) in a straightforward manner:

$$\begin{pmatrix} \boldsymbol{W} \\ p_1 \\ p_2 \\ \dots \end{pmatrix} = \begin{pmatrix} T \\ \boldsymbol{P_1} \\ \boldsymbol{P_2} \\ \dots \end{pmatrix} \cdot \begin{pmatrix} \boldsymbol{\delta N_p}|_{z_2} \\ \delta n_e|_{z_2} \\ \boldsymbol{\delta N_p}|_{z_3} \\ \dots \\ \delta n_e|_{z_k} \end{pmatrix}. \qquad (20)$$

For the example of Eq. (19), $p_i = 0$ while the finite difference approximation of the second derivative is incorporated in the $\boldsymbol{P_i}$ vector. An optimal solution in L^2 norm to this overdetermined equation system can be solved with the method of least squares, resulting in the seeked values for $\left(\boldsymbol{\delta N_p}|_{z_2} \;\; \delta n_e|_{z_2} \;\; \boldsymbol{\delta N_p}|_{z_3} \;\; \dots \;\; \delta n_e|_{z_k} \right)$.

By utilizing weights (regularization parameters) for the equations, their relevance for the solution can be optimized. The customary weighing for the experimental data, such as the equations governed by $\boldsymbol{W}$ and T is performed by multiplying the equation with the inverse of the covariance matrix of the data. If the uncertainty of the data is governed by a Gaussian distribution, this approach gives an optimal result[?] . Setting the regularization parameters for the priors governed by p_i and $\boldsymbol{P_i}$ is less straightforward. A commonly used approximation is setting them so that $\chi^2 = 1$. However, that has been shown to not always lead to optimal results[?] . Therefore, for the reconstructions of the current study, the weight of the different classes of priors corresponding to p_i and $\boldsymbol{P_i}$ have been individually set by hand for every set of experimental data (e.g. for every plasma discharge). In order to mitigate the subjectivity of this approach, a sound approximation for the uncertainty of the reconstructed density data is required.

In this manner, the measurement errors can be incorporated to the reconstruction process. It is noted that results from other diagnostics, such as Thomson scattering and reflectometry can be also incorporated in Eq. (20) if their uncertainty is known.

C. Defining the absolute calibration factor

The detector system does not directly measure $N_2(z)$, but a product of this function and a calibration factor, which differs for every measurement channel. The relative calibration between the channels is usually performed by injecting beam into gas after the plasma discharges and observing the corresponding light profiles. In this case, the emission along the

beam can be taken as constant with reasonable accuracy. Although a more accurate calibration can be performed if the beam attenuation during the gas injection is taken into consideration as well[?] , the low gas pressures and the CMOS image both indicate that this effect is negligibly small for the current system. The angular divergence of the beam is generally negligible due to the focusing system of the the beam injector[?] , this assumption is once again supported by the beam shape as observed by the monitoring CMOS camera. After the relative calibration factor of the channels is defined, one needs to find the absolute calibration factor, α. Directly calculating this quantity is not straightforward as it is dependent on the diagnostic geometry and the parameters of both the optical system and the detectors. Denoting the measured signal with

$$\eta = \alpha N_2(z), \tag{21}$$

Eqs. (16) and (17) can be written as

$$\begin{aligned}\frac{\boldsymbol{\delta N_p}|_{z_{i+1}} - \boldsymbol{\delta N_p}|_{z_i}}{z_{i+1}-z_i} =& \delta n_e|_{z_{i+1}} \boldsymbol{U_p}|_{z_{i+1}} + \boldsymbol{\delta N_p}|_{z_{i+1}} \cdot S_p \\ &+ \left(\frac{\eta|_{z_{i+1}}}{\alpha} - N_2^0|_{z_{i+1}}\right) \boldsymbol{S}_{2p},\end{aligned} \tag{22}$$

$$\begin{aligned}\frac{\left(\frac{\eta|_{z_{i+1}}}{\alpha} - N_2^0|_{z_{i+1}}\right) - \left(\frac{\eta|_{z_i}}{\alpha} - N_2^0|_{z_i}\right)}{z_{i+1}-z_i} =& \delta n_e|_{z_{i+1}} U_2|_{z_{i+1}} \\ &+ \boldsymbol{\delta N_p}|_{z_{i+1}} \cdot \boldsymbol{S}_{p2} + \left(\frac{\eta|_{z_{i+1}}}{\alpha} - N_2^0|_{z_{i+1}}\right) S_{22}\end{aligned} \tag{23}$$

This can be interpreted as a linear equation at every z_i measurement point with an additional unknown, $1/\alpha$. Thus, although the form of the equation changes, the discussion of the previous section remains valid. To avoid false spatiotemporal correlations in the density data due to possible oscillations in the alkali beam current, the absolute calibration factor is obtained separately for each profile during the analysis of large datasets. (For the same purpose, the finite velocity of the beam atoms is taken into consideration as well when obtaining the light profiles.)

D. Implementation of the algorithm

The algorithm was implemented within the Fusion Library of Analysis Packages (FLAP) framework[?] , using the Python programming language. The reconstruction of the density profiles was calculated according to the method described in the preceding sections. In order to utilize the code efficiently, it is also necessary to have a database of solutions as the starting point in Eq. (4).

This database has to contain the values of $\boldsymbol{N^0} \cdot R$ and $n_e^0 R + A$ at the measurement points according to Eq. (8). Moreover, since the collisional rate matrix R is dependent on both the plasma temperature and Z_{eff}, one would need to use different data for different values of these parameters. Nevertheless, the temperature- and Z_{eff}-dependence of the rate matrix for the beam atoms (lithium or sodium) has been found to be weak. Therefore, it has been found sufficiently accurate if only a few versions of the data for different values of the temperatures and Z_{eff} profiles are stored in the database. The atomic collisional rate matrices utilized for this study were taken from [**?**]. The creation of the database for experimental results is further detailed in sections IV A 1 and IV B.

In order to find a light profile in the database sufficiently similar to the measured data, the moments of the light profile were used. On one hand, this approach was chosen, as the moments are independent of the magnitude of the light profiles, which is a necessary feature as the absolute calibration factor is not known before reconstruction. On the other hand, the different moments of the light profile (variation, skewness, kurtosis, etc.) all define different properties of the profile shape. (It is noted that if one were to calculate all infinite moments of the light profile, than that should define its shape completely in certain cases[?] .) For the current task, the second to fifth moments of the $N_2^0(z)$ profiles were calculated when the database of the corresponding data were created. For every measured light profile, its corresponding moments were calculated as well. The profile chosen from the database was the one which had the closest matching moments to the measured data. The first moments of the light profiles were not taken into consideration, as they can be accounted for by shifting the profiles along the beam axis, thus avoiding the need for further increasing the size of the database. Calculations have been performed in order to validate if the moments of light profiles corresponding to similar density profiles are indeed close. The results are not presented herein for brevity, nevertheless it has been found that the moments converge as the density profiles converge to each other, and using the second to fifth moments should be sufficient for the practical identification of similar profiles.

As the reconstructed density profiles are linear combinations of the input data, their uncertainty could be approximated by utilizing the linear uncertainty propagation method. However, this could lead to overly optimistic approximations as there are priors involved in the calculation. In this sense, if one assumes very strong priors for the system, the calculated uncertainties of the density profiles would be very small. To decrease the probability of creating artificially small approximations for the density uncertainty, a more conservative method was utilized: Firstly, the error propagation transfer matrix was calculated using the original Eq. (18), omitting the priors. Secondly, the light profiles corresponding to the reconstructed density profiles were compared with the measured light profiles. Due to the numerical error of the linearization and the usage of priors, these will not align perfectly. The difference between the two light profiles can be used for improving the error approximation of the density: The uncertainty of the measured light profiles is further increased by the difference between the reconstructed and measured light profile data at the corresponding points. The covariance matrix is altered accordingly, and this matrix is the one that gets transformed with the error propagation transfer matrix of Eq. (18). This way the usage of strong priors is counteracted to some level. The resulting approximation is further discussed in section IV A 2.

IV. RESULTS

A. Validation of the method

The validity of the algorithm proposed in this paper has been analyzed utilizing data from the W7-X stellarator. For this purpose, the data from experiment number 20180821.012 was used. (The experiment was aiming at the commissioning of fast ion diagnostics, utilizing the standard magnetic configuration, EJM+252 of W7-X.) Firstly, the A-BES light profile was analyzed using the Bayesian method[?] . The density profile reconstructed this way is plotted on Fig. 3. Since the alkali beam crossed a divertor island for this experiment, the flattening in the density profile is visible at the location of the island[?] .

The density profile obtained from this reconstruction was used to simulate measured light profiles. For this purpose, the light profile corresponding to the reconstructed density was calculated, as shown on the upper plot of Fig. 3. Afterwards some noise was added to the light profile, which was the sum of a Poisson noise (photon noise) and a Gaussian error (e.g. from electric noise). After obtaining reasonably realistic light profiles this way, the density reconstruction algorithm proposed in the current study was used to obtain the electron density profiles. For illustrative purposes, an example for a reconstruction results is shown in Fig. 4. The initial starting profile of this figure has been chosen arbitrarily in order to illustrate the accuracy of the equations of section III.

The data for the continuous line on the lower plot (simulated density profile) corresponds to the data from Fig. 3. Its range has been extended to cover the whole range of major radii, where the diagnostic measures the light intensity. The light profile with the added noise calculated from this density profile is shown in the upper plot. The linearized density reconstruction method requires a database of light profiles and corresponding density profiles. For the current example, a simple database of a single density profile was utilized and its data is also shown in Fig. 4 with dashed lines. (The density profile in the database was created by hand in a way that the results illustrate the limits of the reconstruction accuracy.) The density profiles reconstructed and its corresponding light profile is found to be reasonably accurate in obtaining the original density profile. The reconstructed density matches the original density profile mainly outside the LCFS, but the error approximation for the reconstruction is reliable even further inside the plasma. It is also notable, that the method correctly reconstructed the flattening of the density profile, although the density profile of the initial database contained no such characteristic.

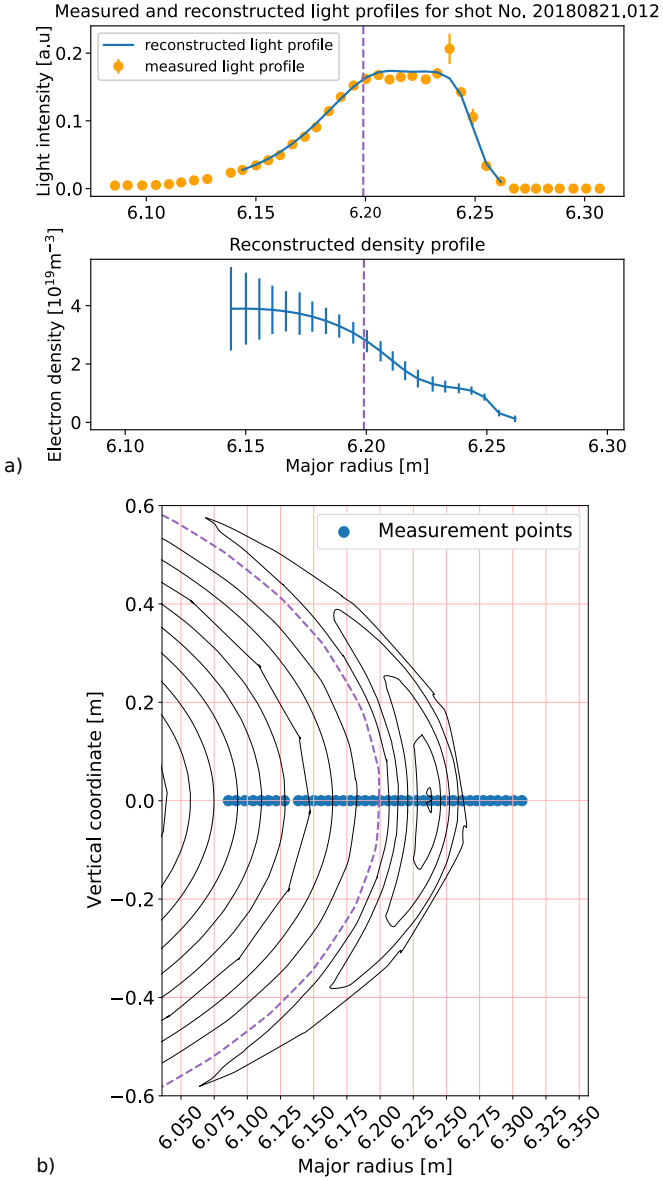

FIG. 3: a) The measured light profile, the reconstructed density profile and its corresponding light profile obtained for the experiment 20180821.012@4s using the Bayesian reconstruction. b) Toroidal cross section of the magnetic surfaces at the beam location. The approximate location of the separatrix between the divertor island and the core plasma is plotted with a dashed purple line in both figures a) and b).

1. *Validity range of the linearized reconstruction method*

A key factor of the applicability of the proposed reconstruction algorithm is the size of the database of initial density profiles and corresponding data it requires to function accurately. Fortunately, the light profiles are only weak functions of Z_{eff}, q and the plasma temperature. Nevertheless, it may be possible that the range of convergence of the linearization method itself is so small that one needs to produce large databases to utilize the algorithm. Although Fig. 4 implies that this is not the case, a more systematic analysis is shown in this section, focusing on the limits of the linearized equation system.

For this purpose, the density profile from Fig. 3 was taken and a random Wiener process with 0 drift and σ_n infinitesimal variance has been added to the density data. This way a new density profile was created. Its value at channel i was

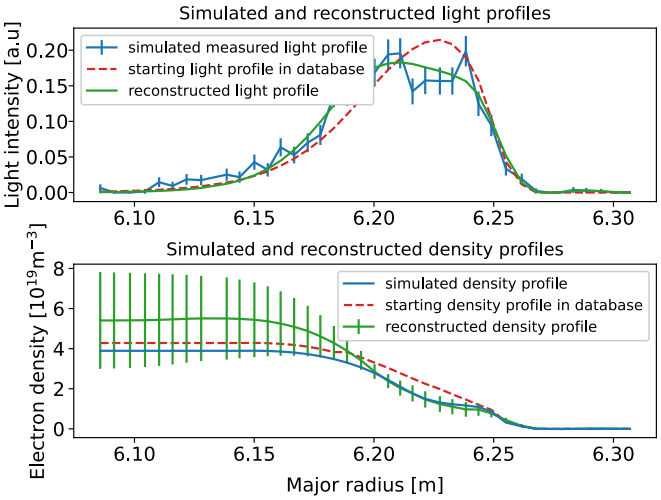

FIG. 4: The simulated, reconstructed light profile and the starting light profile of the linear reconstruction. The corresponding density values are plotted below.

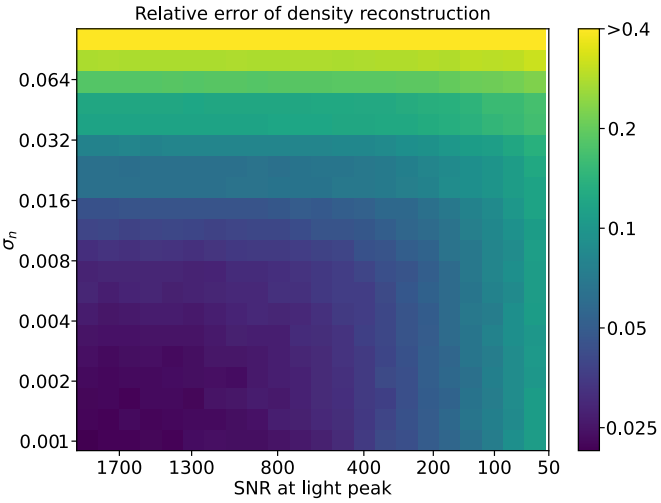

FIG. 5: The relative error of the density reconstruction as a function of SNR at the peak of the light profiles and the distance between the simulated density value and the one in the database.

calculated in the following manner:

$$n_e^{real}|_{z_i} = n_e^0|_{z_i} \cdot (1 + \sigma_n W_{z_i})], \tag{24}$$

where W_{z_i} denotes the value of the Wiener process at z_i. For various values of σ_n, a number of simulated light profiles has been created as in Fig. 3: An additional noise, with variance σ_l, has been added to the light profiles to simulate measurement errors.

Using a database containing only the data corresponding to $n_e^0|_{z_i}$, which in this case is the density profile of Fig. 3, the reconstruction accuracy of $n_e^{real}|_{z_i}$ has been analyzed. The values of both σ_n and σ_l was varied and the accuracy of the reconstruction was calculated, i.e. the difference between the reconstruction results and n_e^{real} of Eq. (24). Although the generated densities n_e^{real} were not necessarily realistic, especially for larger values of σ_n, mathematically the analysis is a useful indicator of the accuracy of the method. Multiple random data profiles have been created for a single value of σ_n and σ_l. The results of performing ≈ 176000 reconstructions are summarized in Fig. 5. For this figure, the relative error of the density reconstruction has been defined as

$$\Delta n_e|_{z_i} = \text{mean}\left(\frac{\left|n_e|_{z_i} - n_e^{real}|_{z_i}\right|}{n_e^{real}|_{z_i}}\right) \tag{25}$$

Channels with $n_e^{real}|_{z_i} = 0$ has been excluded from Eq. (25).

For the plot of Fig. 5, the variance of the light profile has been assumed to predominantly originate from photon noise. There was an additional small Gaussian noise added to the channels to avoid any numerical problems at locations with smaller light intensity. The horizontal axis of the plot was taken to be the SNR at the peak of the light profile. It has been found that the density was reconstructed with a smaller relative error than 10% approximately in the rectangular region of $\sigma_n \leq 0.032$ and $SNR > 100$ at the light peak. For

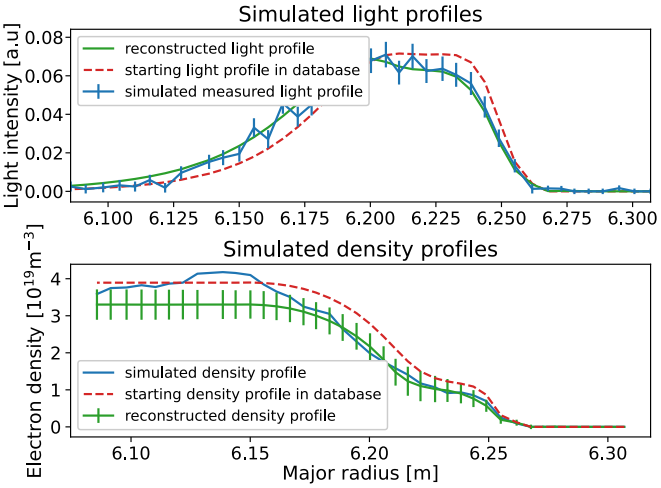

FIG. 6: An example of the results from Fig. 5 with $\sigma_n = 0.0379$ and $SNR \approx 134.5$ at light peak.

illustrative purposes, an example for the generated and reconstructed data just outside this rectangular regime is shown in Fig. 6. These results imply, that the reconstruction accuracy is reasonably good for a large range of parameters. It is noted that both Figs. 4 and 6 indicate that the reconstruction accuracy decreases as the beam propagates into the plasma. This is not a property of the reconstruction algorithm, but is rather inherent to A-BES diagnostics.

A rough estimate for the number of profiles required for the database for the analysis of experimental data is given in the following. For illustrative purposes, one may aim at reconstructing the density profiles with an accuracy of 5%. Firstly, according to Fig. 5 that requires an SNR at the light peak higher than approximately 500, i.e. the relative error at the light peak should be roughly below 5%. Secondly,

for this reconstruction accuracy the limit along the other axis of Fig. 5 is $\sigma_n \leq 0.0089$. This corresponds to a relative difference of approximately 0.03 between the initial and the simulated density profiles. Therefore, assuming that one expects the density values to vary over a magnitude of 10 and that the profile retains its overall shape, one requires approximately $log(10)/log(1.03) \approx 80$ profiles in the initial database to cover the space sufficiently well. Nevertheless, in this case one should also only expect to be able to reconstruct density profiles of similar shapes. For instance, the variation of the profile steepness should be also accounted for in a properly constructed database. When analyzing experimental data, the number of profiles required in the database had to be increased fivefold due to this characteristic. Moreover, since the analysis of different plasma configurations is presumably also required from the algorithm, the generation of a new set of initial profiles for every plasma configuration should be considered as well. Altogether, it has been found that the analysis of the experimental data of W7-X required a database of approximately 9000 initial profiles. Section IV B discusses the construction of this database in more details.

2. *Approximating the reconstruction uncertainty*

A second relevant factor for the applicability of the method is the reliability of the error approximation. For this purpose, the same data were used as for the previous section and the results are plotted in Fig. 7. The horizontal axis refers to the accuracy of light profile reconstruction. The vertical axis is the fraction of the corresponding reconstructed density values for which the difference between the reconstructed and the actual density data were less than the approximated reconstruction uncertainty. The relative error of the light reconstruction is defined similarly as in Eq. (24), but it is normalized with the uncertainty of the simulated light profile data:

$$\Delta\eta = \text{mean}\left(\frac{\left|\alpha N_2|_{z_i} - \eta|_{z_i}\right|}{\sigma(\eta|_{z_i})}\right), \tag{26}$$

where the notation of section III C is utilized: $\alpha N_2|_{z_i}$ denotes the light profile data corresponding to the reconstructed density at z_i and $\sigma(\eta|_{z_i})$ is the simulated uncertainty of the data at this point.

Determining the probability distribution of the reconstruction requires considerable effort, hindering the analysis of Fig. 7. Therefore, a reference horizontal line is plotted on Fig. 7 for the interpretation of the results. This corresponds to the fraction one would obtain if the reconstructed density data were defined by independent Gaussian processes at every measurement point. The results indicate that if this were the case, the error approximation would overapproximate the error bars in the range where the relative light reconstruction error is less than 0.8 and underapproximate it otherwise. The slope of the curve of Fig. 7 is relatively small in the region $\Delta\eta < 0.75$, which is a desirable feature for the interpretation of the error approximation. Hence, a possible interpretation

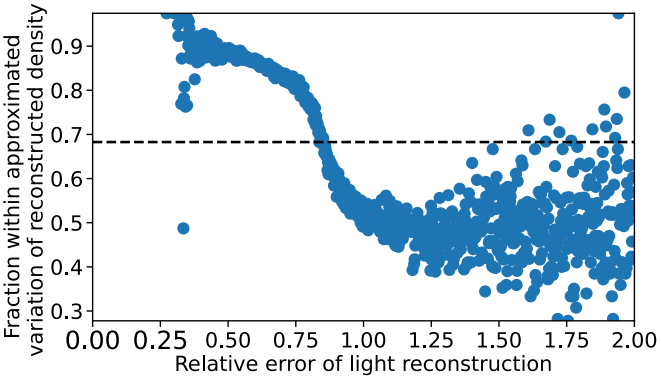

FIG. 7: The fraction of density values within the uncertainty limit as a function of the light reconstruction error.

of the results of Fig. 7 is the following: If the relative light reconstruction error is less than 0.75, then approximately 80% of the actual density data can be expected to be within the approximated uncertainty of the reconstructed density values. For higher reconstruction errors one should not expect the uncertainty approximation to give reliable values.

B. Utilization for experimental data

To illustrate the practical applicability of the presented density reconstruction algorithm, in the following a few results obtained from experimental data is presented. However, a detailed discussion of the observed physical phenomena is out of scope for the current study.

Figure 8 presents the density data obtained for results for experiment 20181017.021, an experiment investigating the MHD activities of the FMM+252 high-iota configuration. A significant feature of this configuration is the presence of internal 5/5 magnetic islands, also shown in Fig. 11b). The temporal resolution of the reconstruction of Fig. 8 is $100\mu s$ and the reconstruction takes about 0.01s - 0.02s per profile with a mid-range PC. From this, about half of the time is required for the calculation itself while the rest is used to search the database of initial profiles for sufficiently similar data. The code has been implemented in Python 3.7 with the usage of only common Python libraries and no robust optimization methods. It is therefore expected that with a sufficiently optimized system, the calculation time could be considerably reduced. For comparison, a number of density profiles from the same experiment were reconstructed with a comparably unoptimized implementation of the Bayesian approach. This method generally required approximately 5s-30s per profile, depending on the number of iterations required for profile convergence. Although the runtime of the latter approach can be also considerably optimized, these runtimes are seen as indicative of the substantially less computational resources required by the linearized method of the current study.

The database of initial profiles was created by taking the source density profile to be defined by the sum of a tangent hyperbolic function and a Gaussian function. The former one

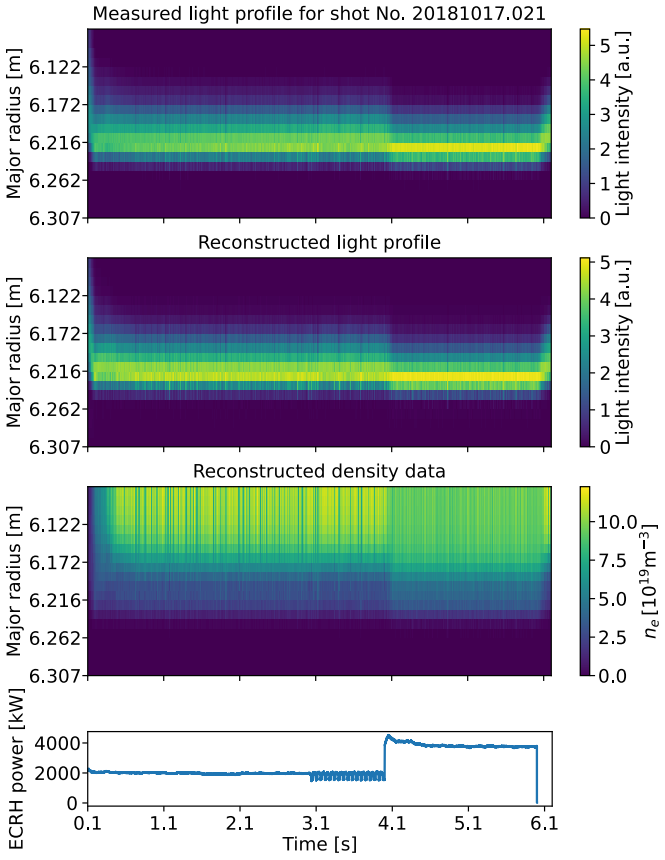

FIG. 8: The measured and reconstructed light profiles with the corresponding density data for experiment 20181017.021 with an additional plot showing the sudden increase of the ECRH power starting at 4s.

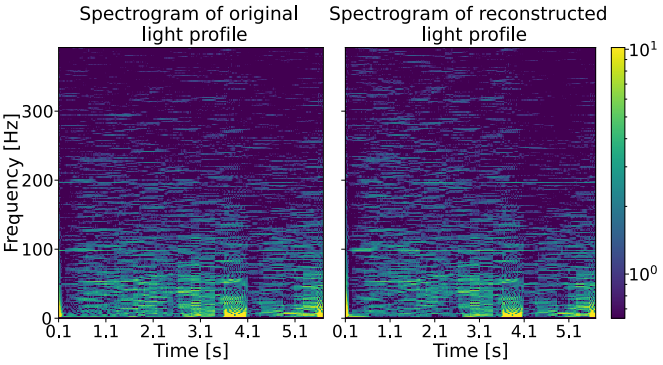

FIG. 9: Spectrogram of data obtained from Fig. 8 for the channel located at a major radius of 6.216m.

corresponds to the overall shape of the density profiles, while the latter function to the additional flattening the magnetic island introduces, as seen in the Bayesian reconstruction of Fig. 3. The properties of these functions were varied over a broad range: The height of the tangent hyperbolic function was varied between $10^{19}m^{-3} - 10^{20}m^{-3}$ (70 different values), the steepness of the tangent hyperbolic profile was varied as well, the transition length from 10%-90% of the inner density was achieved over a distance of $1cm - 15cm$ (5 different values). The variance of the Gaussian function was varied in the range of $1mm - 1cm$ (5 different values) and its relative height in comparison to the height of the tangent hyperbolic function between 0%-30% (5 different values). This range seemed to cover most of the state space adequately. Nevertheless, in a number of cases the density profiles of the database did not match the experiments sufficiently. Thus, approximately 100 additional density profiles based on Bayesian reconstruction data were added to the database as well. It is illustrative for the applicability of the linearized equation system that even this relatively straightforward method of creating the database has been found to perform adequately for the analysis of all 33 experiments for which the linearized algorithm has been used for.

Figure 8 implies highly similar measured and fitted light profiles. For instance, the effects of a sudden increase in the electron-cyclotron-resonance heating? (ECRH) power from 2MW to 4MW at 4s is clearly seen on both light profiles. For further analysis, the temporal spectrogram of the measured and reconstructed light data at the channel near their light peaks ($R = 6.216$m) is presented in Fig. 9. These have been found to correspond reasonably well also. The color range of the figures has been set to emphasize the difference between the two results. The main difference occurs for frequencies above $\approx$ 200Hz, where the fluctuations in the measurement data are weak. The data before $\approx$ 1.1s shows that the reconstructed light profile has more prominent oscillations in this frequency window. This is presumably due to the finite amount of profiles used in the initialization database. As the light profiles evolve in time, the algorithm also switches repeatedly between the initial profiles it uses for the density calculation. This is expected to add noise to the reconstructed density and light data. On the other hand, for the time window at around 5.1s, it is the original data that has more prominent high-frequency components. This is probably due to the smoothing effect of the priors. Although neither of these effects are pronounced, they indicate that the algorithm presented in this study should be applied to small perturbations cautiously as the density reconstruction can produce artificial noise and it may also flatten out actual density perturbations.

As the reconstruction is reasonably fast, the algorithm can be used for the analysis of density fluctuations directly. An example for this is shown in Figs. 10 and 11. Figure 10 shows the data of experiment 20181017.021 for the time window [2.7s, 3.5s]. The light profiles indicate an oscillation at the plasma edge. Filtering the density data for [10 Hz,1000 Hz] and calculating the temporal cross-correlation for the channel located at a major radius of 6.221m, one obtains Fig. 11a) showing a 20Hz periodicity in the results. It is noted that the major radius of 6.221m corresponds to the channel closest to the approximate location of the peak of the observed light profiles. A phase inversion can be observed at this location in the light data, which is a consequence of the beam attenuation effect? . A jump in the correlation sign can be observed at a major radius of approximately 6.18m in the density data as well. Previous studies implied that comparable behavior may occur at the LCFS? . Based on field line tracer calculations?

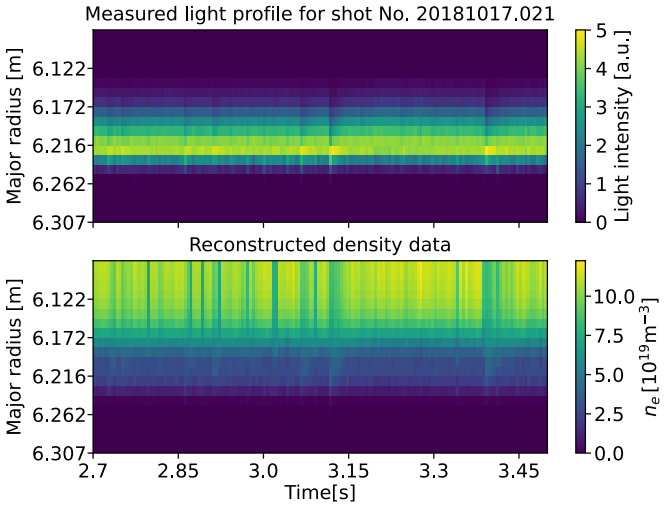

FIG. 10: The measured light data and reconstructed density data for experiment 20181017.021.

shown in Fig. 11b), the internal magnetic island can be found between major radii [6.16m, 6.205m] with an O point located at 6.182m. Therefore, it is presumed that the jump in the spatiotemporal correlation of the density profiles occurs at the inner interface between the magnetic island and the inner flux surfaces. It is however noted that at the point of the phase inversion the reconstruction accuracy is considerably worse than at larger major radii. Thus, artificial fluctuations may also appear in the data at this point. Drawing a conclusive interpretation of the results therefore necessitates further analysis, preferably a comparison with data from other diagnostics.

Although the correlation of Fig. 11a) starts to oscillate at channels outside $R \approx 6.25m$, this is a numerical artifact. In this region the reconstructed density values are close to machine precision. Also, the correlation data indicate that the density perturbations are spreading inwards through the divertor island. Although a detailed analysis of the physical process behind the results is out of scope of the current study, they are possibly related to the low-frequency oscillations observed at the plasma edge for similar plasma configurations[?] .

V. SUMMARY

The study presented a new density reconstruction algorithm for the alkali beam spectroscopy diagnostic. It is based on the linearization of the governing differential equations, resulting in direct calculations while also allowing the incorporation of priors to the reconstruction. The applicability of the code has been tested against simulated data and experimental results as well. It has been found that it gives accurate predictions to the density profiles and a database of limited size is sufficient for its application to the analysis of experimental data. An error propagation method has been developed using the linear propagation of uncertainties. Its applicability has also been tested and it has been found to be a suitable indicator for the accuracy of the results as long as the measured and reconstructed light profiles match sufficiently.

Setting up the linear equation system and solving it requires approximately 0.02s on a general purpose mid-range PC for the code implemented in Python. This has been found to be 2-3 orders of magnitude less than required by the traditional Bayesian method, while retaining the statistical approach to the problem. For extensive databases of initial profiles, determining the starting point of the calculation has been found to require a comparable amount of computational time as the reconstruction itself as long as the former task is not optimized. Due to the reasonable amount of time that the reconstruction takes, it is also possible to analyze the density data of experimental results with a high time resolution to which a few examples have been given. This can be a welcome feature for the analysis of plasma edge turbulence using A-BES data.

ACKNOWLEDGMENTS

This work has been carried out within the framework of the EUROfusion Consortium and has received funding from the Euratom research and training programme 2014-2018 and 2019-2020 under grant agreement No 633053. The views and opinions expressed herein do not necessarily reflect those of the European Comission.

DATA AVAILABILITY

The data that support the findings of this study are available from the corresponding author upon reasonable request.

REFERENCES

[1]E Wolfrum, F Aumayr, D Wutte, HP Winter, E Hintz, D Rusbüldt, and RP Schorn. Fast lithium-beam spectroscopy of tokamak edge plasmas. *Review of scientific instruments*, 64(8):2285–2292, 1993.

[2]S Zoletnik, G Anda, M Aradi, O Asztalos, S Bató, A Bencze, M Berta, G Demeter, D Dunai, P Hacek, et al. Advanced neutral alkali beam diagnostics for applications in fusion research. *Review of Scientific Instruments*, 89(10):10D107, 2018.

[3]DM Thomas. Development of lithium beam emission spectroscopy as an edge fluctuation diagnostic for DIII-D. *Review of Scientific Instruments*, 66(1):806–811, 1995.

[4]K McCormick, S Fiedler, G Kocsis, J Schweinzer, and S Zoletnik. Edge density measurements with a fast Li beam probe in tokamak and stellarator experiments. *Fusion Engineering and Design*, 34:125–134, 1997.

[5]G Anda, A Bencze, M Berta, D Dunai, P Hacek, J Krbec, DI Réfy, T Krizsanóczi, S Bató, T Ilkei, et al. Lithium beam diagnostic system on the COMPASS tokamak. *Fusion Engineering and Design*, 108:1–6, 2016.

[6]DI Réfy, M Brix, R Gomes, B Tál, S Zoletnik, D Dunai, G Kocsis, S Kálvin, T Szabolics, and JET Contributors. Sub-millisecond electron density profile measurement at the JET tokamak with the fast lithium beam emission spectroscopy system. *Review of Scientific Instruments*, 89(4):043509, 2018.

[7]S Zoletnik, GH Hu, B Tál, D Dunai, G Anda, O Asztalos, GI Pokol, S Kálvin, J Németh, and T Krizsanóczi. Ultrafast two-dimensional lithium beam emission spectroscopy diagnostic on the EAST tokamak. *Review of Scientific Instruments*, 89(6):063503, 2018.

[8]G Anda, D Dunai, T Krizsanóczi, D Nagy, M Otte, S Hegedűs, M Vécsei, S Zoletnik, G Gardonyi, et al. Measurement of edge plasma parameters at

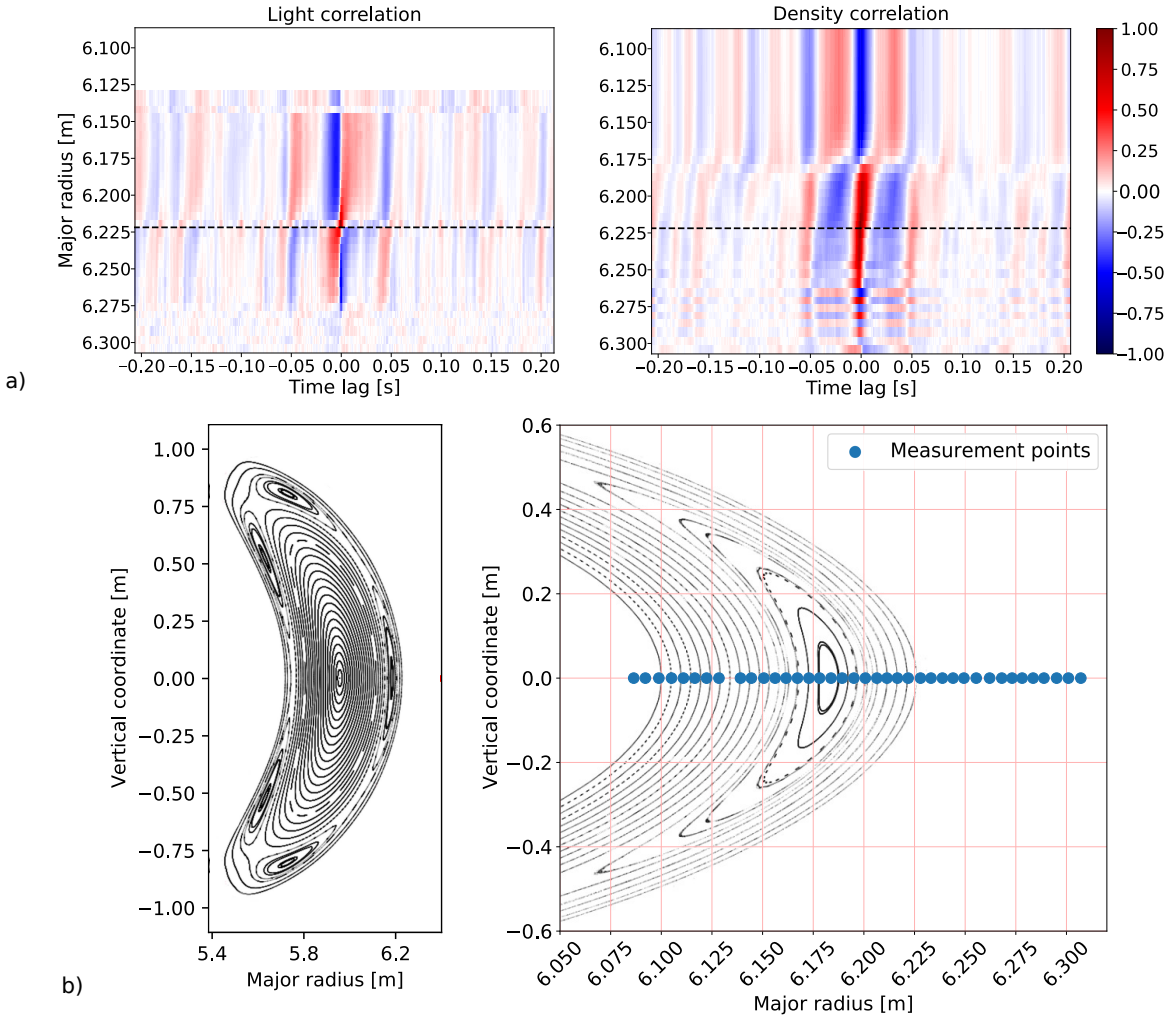

FIG. 11: a) The cross correlation of the light and density data at the channel located at $R \approx 6.221m$ (denoted with a dashed horizontal line) as a function of major radius and time lag. b) Left: The closed magnetic surfaces at the toroidal cross section of the beam injection for the FMM+252 configuration of experiment 20181017.021. Right: A magnified section of the same torodial cross section focusing on the magnetic island and the measurement points of the detector.

W7-X using alkali beam emission spectroscopy. *Fusion Engineering and Design*, 146:1814–1819, 2019.

[9] G Anda, D Dunai, M Lampert, T Krizsanóczi, J Németh, S Bató, YU Nam, GH Hu, and S Zoletnik. Development of a high current 60 keV neutral lithium beam injector for beam emission spectroscopy measurements on fusion experiments. *Review of Scientific Instruments*, 89(1):013503, 2018.

[10] D Dunai, S Zoletnik, J Sárközi, and AR Field. Avalanche photodiode based detector for beam emission spectroscopy. *Review of Scientific Instruments*, 81(10):103503, 2010.

[11] M Lampert, G Anda, A Czopf, G Erdei, D Guszejnov, Á Kovácsik, GI Pokol, DI Réfy, YU Nam, and S Zoletnik. Combined hydrogen and lithium beam emission spectroscopy observation system for Korea Superconducting Tokamak Advanced Research. *Review of Scientific Instruments*, 86(7):073501, 2015.

[12] M Berta, G Anda, A Bencze, D Dunai, P Háček, M Hron, A Kovácsik, J Krbec, R Pánek, DI Réfy, et al. Li-BES detection system for plasma turbulence measurements on the COMPASS tokamak. *Fusion Engineering and Design*, 96:795–798, 2015.

[13] G Birkenmeier, P Manz, D Carralero, FM Laggner, G Fuchert, K Krieger, H Maier, F Reimold, K Schmid, R Dux, et al. Filament transport, warm ions and erosion in ASDEX Upgrade L-modes. *Nuclear Fusion*, 55(3):033018, 2015.

[14] L Bardoczi, TA Carter, RJ La Haye, TL Rhodes, and GR McKee. Impact of neoclassical tearing mode–turbulence multi-scale interaction in global confinement degradation and magnetic island stability. *Physics of Plasmas*, 24(12):122503, 2017.

[15] R Fischer, E Wolfrum, J Schweinzer, et al. Probabilistic lithium beam data analysis. *Plasma Physics and Controlled Fusion*, 50(8):085009, 2008.

[16] A Pavone, J Svensson, S Kwak, M Brix, RC Wolf, and JET Contributors. Neural network approximated Bayesian inference of edge electron density profiles at JET. *Plasma Physics and Controlled Fusion*, 62(4):045019, 2020.

[17] AC Aitken. VI.—On the graduation of data by the orthogonal polynomials of least squares. *Proceedings of the Royal Society of Edinburgh*, 53:54–78, 1934.

[18] W.Clem Karl. 3.6 - Regularization in Image Restoration and Reconstruction. In Al Bovik, editor, *Handbook of Image and Video Processing*, Communications, Networking and Multimedia. Academic Press, Burlington, second edition, 2005.

[19] K Yamamoto, K Yamamura, K Sato, T Ota, H Suzuki, and S Ohsuka. Development of multi-pixel photon counter (MPPC). In *2006 IEEE Nuclear Science Symposium Conference Record*, volume 2, pages 1094–1097. IEEE, 2006.

[20]J Schweinzer, E Wolfrum, F Aumayr, M Pockl, H Winter, RP Schorn, E Hintz, and A Unterreiter. Reconstruction of plasma edge density profiles from Li I (2s-2p) emission profiles. *Plasma physics and controlled fusion*, 34(7):1173, 1992.

[21]W von der Linden. Maximum-entropy data analysis. *Applied Physics A*, 60(2):155–165, 1995.

[22]Richard CA, Brian B, and Clifford HT. 5 Tikhonov regularization. In *Parameter Estimation and Inverse Problems*, volume 90 of *International Geophysics*, pages 89–118. Academic Press, 2005.

[23]CF Gauss. *Theoria motus corporum coelestium in sectionibus conicis solem ambientium auctore Carolo Friderico Gauss*. sumtibus Frid. Perthes et IH Besser, 1809.

[24]S Zoletnik, G Cseh, Ö Asztalos, M Lampert, G.I. Pokol, and M Vécsei. Fusion Library of Analysis Packages. https://github.com/fusion-flap/flap, 2019.

[25]K Igenbergs, J Schweinzer, Igor Bray, D Bridi, and F Aumayr. Database for inelastic collisions of sodium atoms with electrons, protons, and multiply charged ions. *Atomic Data and Nuclear Data Tables*, 94(6):981–1014, 2008.

[26]JA Shohat and JD Tamarkin. *The problem of moments*. Number 1. American Mathematical Soc., 1943.

[27]RC Wolf, S Bozhenkov, A Dinklage, G Fuchert, YO Kazakov, HP Laqua, S Marsen, NB Marushchenko, T Stange, M Zanini, et al. Electron-cyclotron-resonance heating in Wendelstein 7-X: A versatile heating and current-drive method and a tool for in-depth physics studies. *Plasma Physics and Controlled Fusion*, 61(1):014037, 2018.

[28]M Willensdorfer, G Birkenmeier, R Fischer, FM Laggner, E Wolfrum, G Veres, F Aumayr, D Carralero, L Guimarais, B Kurzan, et al. Characterization of the Li-BES at ASDEX Upgrade. *Plasma Physics and Controlled Fusion*, 56(2):025008, 2014.

[29]S Zoletnik, M Anton, M Endler, S Fiedler, M Hirsch, K McCormick, J Schweinzer, and W7-AS team. Density fluctuation phenomena in the scrape-off layer and edge plasma of the Wendelstein 7-AS stellarator. *Physics of Plasmas*, 6(11):4239–4247, 1999.

[30]SA Bozhenkov, J Geiger, M Grahl, J Kisslinger, A Werner, and RC Wolf. Service oriented architecture for scientific analysis at W7-X. An example of a field line tracer. *Fusion Engineering and Design*, 88(11):2997–3006, 2013.

[31]GA Wurden, S Ballinger, S Bozhenkov, C Brandt, B Buttenschoen, M Endler, S Freundt, K Hammond, M Hirsch, U Hoefel, et al. Quasi-continuous low frequency edge fluctuations in the W7-X stellarator. In *45th EPS Conference on Plasma Physics*. European Physical Society, 2018.